

Planet-star interactions with precise transit timing

III. Entering the regime of dynamical tides^{***}

G. Maciejewski¹, M. Fernández², A. Sota², P. J. Amado², D. Dimitrov³, Y. Nikolov³, J. Ohlert^{4,5}, M. Mugrauer⁶, R. Bischoff⁶, T. Heyne⁶, F. Hildebrandt⁶, W. Stenglein⁶, A. A. Arévalo⁷, S. Neira⁷, L. A. Riesco⁷, V. Sánchez Martínez⁷, and M. M. Verdugo⁷

¹ Institute of Astronomy, Faculty of Physics, Astronomy and Informatics, Nicolaus Copernicus University in Toruń, Grudziadzka 5, 87-100 Toruń, Poland, e-mail: gmac@umk.pl

² Instituto de Astrofísica de Andalucía (IAA-CSIC), Glorieta de la Astronomía 3, 18008 Granada, Spain

³ Institute of Astronomy and National Astronomical Observatory, Bulgarian Academy of Sciences, 72 Tsarigradsko Chaussee Blvd., 1784, Sofia, Bulgaria

⁴ Michael Adrian Observatorium, Astronomie Stiftung Trebur, 65428 Trebur, Germany

⁵ University of Applied Sciences, Technische Hochschule Mittelhessen, 61169 Friedberg, Germany

⁶ Astrophysikalisches Institut und Universitäts-Sternwarte, Schillergässchen 2, 07745 Jena, Germany

⁷ Valencia International University, Spain

Received — ; accepted —

ABSTRACT

Context. Hot Jupiters on extremely short-period orbits are expected to be unstable to tidal dissipation and spiral toward their host stars. That is because they transfer the angular momentum of the orbital motion through tidal dissipation into the stellar interior. Although the magnitude of this phenomenon is related to the physical properties of a specific star-planet system, statistical studies show that tidal dissipation might shape the architecture of hot Jupiter systems during the stellar lifetime on the main sequence.

Aims. The efficiency of tidal dissipation remains poorly constrained in star-planet systems. Stellar interior models show that the dissipation of dynamical tides in radiation zones could be the dominant mechanism driving planetary orbital decay. These theoretical predictions can be verified with the transit timing method.

Methods. We acquired new precise transit mid-times for five planets. They were previously identified as the best candidates for which orbital decay might be detected. Analysis of the timing data allowed us to place tighter constraints on the orbital decay rate.

Results. No statistically significant changes in their orbital periods were detected for all five hot Jupiters in systems HAT-P-23, KELT-1, KELT-16, WASP-18, and WASP-103. For planets HAT-P-23 b, WASP-18 b, and WASP-103 b, observations show that the mechanism of the dynamical tides dissipation probably does not operate in their host stars, preventing them from rapid orbital decay. This finding aligns with the models of stellar interiors of F-type stars, in which dynamical tides are not fully damped due to convective cores. For KELT-16 b, the span of transit timing data was not long enough to verify the theoretical predictions. KELT-1 b was identified as a potential laboratory for studying the dissipative tidal interactions of inertial waves in a convective layer. Continued observations of those two planets may provide further empirical verification of the tidal dissipation theory.

Key words. stars: individual: HAT-P-23, KELT-1, KELT-16, WASP-18, WASP-103 – planets and satellites: individual: HAT-P-23 b, KELT-1 b, KELT-16 b, WASP-18 b, WASP-103 b – methods: observational – techniques: photometric – time

1. Introduction

The statistical studies of the planetary systems harbouring hot Jupiters provide substantial evidence of dissipative tidal interactions between those massive planets and their host stars. In a typical configuration, in which the host star rotates slower than its close planetary companion orbits it, the angular momentum of the orbital motion is transferred into the stellar spin due to tidal

dissipation in the stellar interior. The population of hot Jupiter host stars was found to have a lower Galactic velocity dispersion than the field stars in a reference sample (Hamer & Schlaufman 2019). This kinematical youth suggests that their planets must spiral in due to tidal interactions in time scales noticeably shorter than the stellar evolution on the main sequence. Furthermore, the host stars with close-orbiting giant planets tend to be younger in gyro-chronological dating compared to their ages determined from stellar-evolutionary models (Brown 2014; Maxted et al. 2015; Tejada Arevalo et al. 2021). They are supposed to rotate faster because their spiralling-in planets have spun them up.

The magnitude of tidal dissipation in a star is quantified by a modified tidal quality factor defined as

$$Q'_\star = \frac{2\pi E_{\text{tide}}}{\oint D dt} \frac{3}{2k_2}, \quad (1)$$

* This research is partly based on (1) data obtained at the 1.5m telescope of the Sierra Nevada Observatory (Spain), which is operated by the Consejo Superior de Investigaciones Científicas (CSIC) through the Instituto de Astrofísica de Andalucía, (2) observations collected with telescopes at the Rozhen National Astronomical Observatory, and (3) observations obtained with telescopes of the University Observatory Jena, which is operated by the Astrophysical Institute of the Friedrich-Schiller-University.

** The light curves will be available at the CDS.

where E_{tide} is the maximum energy stored in the tide, D is the dissipation integrated over the tidal period P_{tide} , and k_2 is the second-order potential Love number (Barker 2020). The tidal period is related to the stellar rotation period P_{\star} and planetary orbital period P_{orb} with the formula

$$\frac{1}{P_{\text{tide}}} = 2 \left(\frac{1}{P_{\text{orb}}} - \frac{1}{P_{\star}} \right). \quad (2)$$

The value of Q'_{\star} encompasses the physical properties of the specific star-planet system. Hence it might significantly vary from one system to another and makes us take the results of population-wide studies of hot-Jupiters as a rather rough approximation (Barker 2020).

The stellar interior might dissipate the tidal energy under the equilibrium (EQ) and dynamical regimes. In the former, the global-scale flow is induced by the hydrostatic response of the stellar figure over the planet's gravitational potential. Those tides are dissipated in a convective layer¹. The efficiency of this mechanism is, however, low for main-sequence stars, resulting in its component of the modified tidal quality factor of $Q'_{\star, \text{EQ}} > 10^{10}$ (Barker 2020). In the dynamical regime, internal gravity waves (IGW) in radiation layers or inertial waves (IW) in convective layers are excited in response to tidal forcing. Calculations show that these mechanisms can be efficient in tidal dissipating under favourable conditions in which non-adiabatic or non-linear effects can operate. Dissipation of internal gravity waves in radiation layers might be substantially enhanced, resulting in $Q'_{\star, \text{IGW}}$ of the order of 10^6 for main-sequence F-type stars, and even as low as $10^5 - 10^6$ for $0.4 M_{\odot}$ at the same evolutionary stage (Barker 2020). Dissipation due to inertial waves in convective layers only operates if $P_{\text{tide}} > 2P_{\star}$, and might yield $Q'_{\star, \text{IW}}$ as low as $10^5 - 10^6$ for fast-rotating stars with masses below $1.1 M_{\odot}$ (Barker 2020). Dissipation of the equilibrium tides seems to be too weak to have observable effects in individual planetary systems. On the other hand, the magnitude of dynamical tides dissipation could manifest as orbital decay detectable in decadal timescales for favourable systemic configurations.

In our previous papers (Maciejewski et al. 2018, 2020), we used the transit timing method to probe values of Q'_{\star} for a sample of systems with massive planets on extremely tight orbits. We selected them among the candidates for which orbital decay due to tidal dissipation might be detected over a decade if their modified tidal quality factors were 10^6 . In this study, we extend the time coverage of observations for five systems HAT-P-23 (Fulton et al. 2011), KELT-1 (Siverd et al. 2012), KELT-16 (Oberst et al. 2017), WASP-18 (Hellier et al. 2009), and WASP-103 (Gillon et al. 2014) using both high-quality ground-based follow-up observations and photometric time series from the Transiting Exoplanet Survey Satellite (TESS, Ricker et al. 2014). The data sets with homogeneously determined mid-transit times allowed us to place tighter constraints on the values of Q'_{\star} in these systems and explore the dynamical tides' regime.

2. Observations and data reduction

2.1. Ground-based observations

We acquired ten transit light curves for HAT-P-23 b, five for KELT-1 b, ten for KELT-16 b, and eight for WASP-103 b (including two light curves of the transit observed on 2019

¹ The contribution of dissipation in a convective core is predicted to be negligibly small (Barker 2020)

June 01). We employed six instruments: the 2.0 m Ritchey-Chrétien-Coudé telescope (Rozhen) at the National Astronomical Observatory Rozhen (Bulgaria) equipped with a Roper Scientific VersArray 1300B CCD camera; the 1.5 m Ritchey-Chrétien telescope (OSN150) at the Sierra Nevada Observatory (OSN, Spain) with a Roper Scientific VersArray 2048B CCD camera; the 1.2 m Trebur one-meter telescope (Trebur) at the Michael Adrian Observatory in Trebur (Germany) with an SBIG STL-6303 CCD camera; the 0.9 m Ritchey-Chrétien telescope (OSN90) at OSN with a Roper Scientific VersArray 2048B CCD camera; the 0.9/0.6 m Schmidt Teleskop Kamera (Jena, Mugrauer & Berthold 2010) at the University Observatory Jena (Germany); and the 0.6 m Cassegrain photometric telescope (Torun) at the Institute of Astronomy of the Nicolaus Copernicus University in Toruń (Poland) with an FLI 16803 CCD camera.

The telescope defocusing technique, in which the stellar point spread function is broadened, spreading starlight over many CCD pixels, was used at each instrument. It reduces flat-fielding errors and minimises the amount of observing time lost for CCD readout (e.g. Southworth et al. 2009). The observations were primarily performed without any filter to maximise the signal-to-noise ratio for precise transit timing, and only occasionally were the observations acquired through an *R*-band filter. The only exception is KELT-1, the brightest star in our sample ($G \approx 10.6$ mag). For that field, photometric time series were secured with the *R* filter to avoid saturation of the target and comparison stars. If available, auto-guiding was applied to minimise field drifts during each run. Otherwise, tracking corrections were applied manually to keep stellar images around the fixed position in a CCD matrix within $\approx 5''$.

The observations were scheduled to secure 60-90 minutes of out-of-transit monitoring before and after each transit to remove trends reliably. For several light curves, data portions were lost due to unfavourable weather conditions or observing constraints. Details on the individual observing runs are collected in Table 1.

AstroImageJ (Collins et al. 2017) was used for data processing and photometric extraction of the final light curves. The science frames were preprocessed following a standard procedure, including de-biasing or dark-current correction and flat-fielding with sky flat-field frames. The timestamps of mid-exposures were transformed into barycentric Julian dates and barycentric dynamical time BJD_{TDB} using a built-in converter. Fluxes were obtained with the aperture photometry method with the aperture size and ensemble of comparison stars optimised in trial iterations. Then, normalisation to unity outside the transit was performed simultaneously with a trial transit model and de-trending against airmass, time, and seeing². The final light curves are plotted in Figs. 1–4.

2.2. TESS observations

Three systems of our sample, KELT-1, KELT-16, and WASP-18, were observed with the Transiting Exoplanet Survey Satellite (TESS, Ricker et al. 2014) in a 2-minute cadence mode. The photometric time series were extracted from Pre-search Data Conditioning Simple Aperture Photometry which is available via the exo.MAST portal³. The details on individual observing runs are given in Table 2.

The Savitzky-Golay filter implemented in the Lightkurve package (ver. 2.0, Lightkurve Collaboration et al. 2018) was

² Thanks to precise guiding, trends against the X-Y position on a CCD matrix were neglectable.

³ <https://exo.mast.stsci.edu>

Table 1. Details on the observing runs.

Date UT (Epoch)	Telescope	Band	UT start–end	X	N_{obs}	t_{exp} (s)	Γ	pnr (ppth)
HAT-P-23 b								
2019 Sep 17 (3209)	Jena	clear	20:08–23:31	1.21 \rightarrow 1.73	211	45	1.05	1.51
2019 Oct 15 (3232)	Jena	clear	17:43–20:52	1.21 \rightarrow 1.49	144	45	1.07	2.13
2020 Jul 21 (3463)	Trebur	clear	21:17–01:56	1.41 \rightarrow 1.19 \rightarrow 1.34	240	60	0.87	0.93
2020 Aug 07 (3477)	OSN150	R	20:32–01:15	1.40 \rightarrow 1.07 \rightarrow 1.16	761	20	2.68	0.99
2020 Oct 14 (3533)	OSN150	clear	18:57–00:00	1.07 \rightarrow 2.60	710	20	2.35	1.58
2021 Jul 04 (3750)	OSN90	clear	23:15–03:27	1.28 \rightarrow 1.07 \rightarrow 1.16	422	30	1.67	0.91
2021 Jul 09 (3754)	Rozhen	clear	20:41–00:15	1.40 \rightarrow 1.10 \rightarrow 1.12	458	20	2.39	0.70
2021 Jul 15 (3759)	OSN90	clear	21:41–02:24	1.52 \rightarrow 1.07 \rightarrow 1.12	474	30	1.67	1.03
2021 Aug 01 (3773)	OSN90	clear	22:07–01:46	1.17 \rightarrow 1.07 \rightarrow 1.17	285	40	1.31	1.22
2021 Sep 04 (3801)	OSN150	clear	20:09–00:56	1.14 \rightarrow 1.07 \rightarrow 1.47	677	20	2.35	0.65
KELT-1 b								
2020 Oct 11 (2649)	OSN90	R	20:21–00:56	1.15 \rightarrow 1.00 \rightarrow 1.10	457	30	1.67	0.96
2020 Oct 28 (2663)	OSN90	R	20:36–02:08	1.03 \rightarrow 1.00 \rightarrow 1.57	549	30	1.67	0.82
2021 Sep 01 (2916)	OSN150	R	21:59–02:49	1.32 \rightarrow 1.00 \rightarrow 1.04	1002	15	3.47	0.80
2021 Sep 29 (2939)	OSN90	R	21:42–02:31	1.09 \rightarrow 1.00 \rightarrow 1.20	481	30	1.67	0.86
2021 Oct 10 (2948)	OSN90	R	20:42–01:34	1.12 \rightarrow 1.00 \rightarrow 1.16	242	30	1.67	0.79
KELT-16 b								
2019 Aug 14 (1510)	Toruń	clear	20:05–00:28	1.17 \rightarrow 1.07 \rightarrow 1.18	508	27	2.00	1.48
2020 Jul 22 (1864)	OSN90	clear	21:00–01:22	1.57 \rightarrow 1.00 \rightarrow 1.01	385	35	1.47	1.08
2020 Aug 20 (1894)	Trebur	clear	22:36–03:01	1.05 \rightarrow 1.67	257	50	1.02	0.87
2020 Aug 21 (1895)	OSN90	clear	21:24–01:45	1.08 \rightarrow 1.00 \rightarrow 1.19	337	40	1.31	0.70
2020 Aug 22 (1896)	OSN90	clear	20:44–01:01	1.15 \rightarrow 1.00 \rightarrow 1.10	336	40	1.31	0.81
2020 Aug 23 (1897)	OSN90	clear	19:48–00:19	1.30 \rightarrow 1.00 \rightarrow 1.05	353	40	1.31	0.72
2021 Aug 30 (2281)	OSN90	clear	22:05–03:07	1.01 \rightarrow 1.00 \rightarrow 1.75	678	20	2.31	1.02
2021 Aug 31 (2282)	Trebur	clear	22:09–02:08	1.06 \rightarrow 1.60	244	50	1.02	0.78
2021 Sep 02 (2284)	OSN150	R	20:00–00:51	1.15 \rightarrow 1.00 \rightarrow 1.17	639	25	2.20	0.90
2021 Oct 04 (2317)	OSN90	clear	19:39–00:52	1.01 \rightarrow 1.00 \rightarrow 1.78	320	40	1.31	1.01
WASP-103 b								
2019 May31 (2351)	OSN150	clear	22:17–03:36	1.31 \rightarrow 1.15 \rightarrow 1.72	422	40	1.32	0.84
2019 Jun 01 (2352)	OSN150	clear	20:55–02:30	1.69 \rightarrow 1.15 \rightarrow 1.38	398	40	1.19	0.92
	Jena	clear	21:31–00:27	1.51 \rightarrow 1.31 \rightarrow 1.45	183	45	1.05	1.75
2019 Jun 26 (2379)	Trebur	clear	21:14–01:07	1.37 \rightarrow 1.36 \rightarrow 1.99	195	55	0.95	1.39
2019 Jun 27 (2380)	Rozhen	clear	19:17–23:19	1.28 \rightarrow 1.21 \rightarrow 1.55	463	26	1.93	0.86
2021 May 21 (3130)	OSN150	R	23:45–03:15	1.20 \rightarrow 1.15 \rightarrow 1.39	230	50	1.15	1.82
2021 Jun 03 (3144)	OSN150	R	21:44–00:49	1.37 \rightarrow 1.15 \rightarrow 1.18	205	50	1.15	1.24
2021 Jul 12 (3186)	Rozhen	clear	19:01–23:16	1.23 \rightarrow 1.21 \rightarrow 1.97	597	20	2.39	0.71

Notes. Date UT is given for the beginning of an observing run. Epoch is the transit number from the initial ephemeris given in the discovery papers. X tracks the target’s airmass during a run. N_{obs} is the number of useful scientific exposures. t_{exp} is the exposure time used. Γ is the median number of exposures per minute. pnr is the photometric noise rate (Fulton et al. 2011) in parts per thousand (ppth) of the normalised flux per minute of observation.

Table 2. Details on the TESS observations used.

System	Sector	Camera	from – to (UT)	N_{obs}	pnr (ppth)	N_{tr}
KELT-1	17	2	2019 Oct 07 – 2019 Nov 02	12892	1.67	14
KELT-16	15	1	2019 Aug 15 – 2019 Sep 11	13129	3.76	18
	41	1	2021 Jul 23 – 2021 Aug 20	18322	4.12	26
WASP-18	29	2	2020 Aug 26 – 2020 Sep 22	14361	0.79	21
	30	2	2020 Sep 22 – 2020 Oct 21	16573	0.78	24

Notes. N_{obs} is the number of useful data points. pnr is the photometric noise rate. N_{tr} is the number of complete transit light curves used in this study.

used to remove any low-frequency trends from astrophysical or systematic effects on time scales much longer than the expected transit duration. Data points falling in transits and occultations were masked out using preliminary transit ephemerides. Since the durations of the transits were 2.1–2.7 hours, the length of the filter window was set to 6 hours. Measurements with fluxes or

flux errors listed as NaN were automatically removed. Apparent outliers were identified by visual inspection and then rejected. The light curves of complete transits within some time margins before and after each transit were extracted for further analysis. The length of these margins was set as twice the transit duration. The phase-folded transit light curves are shown in Fig. 5.

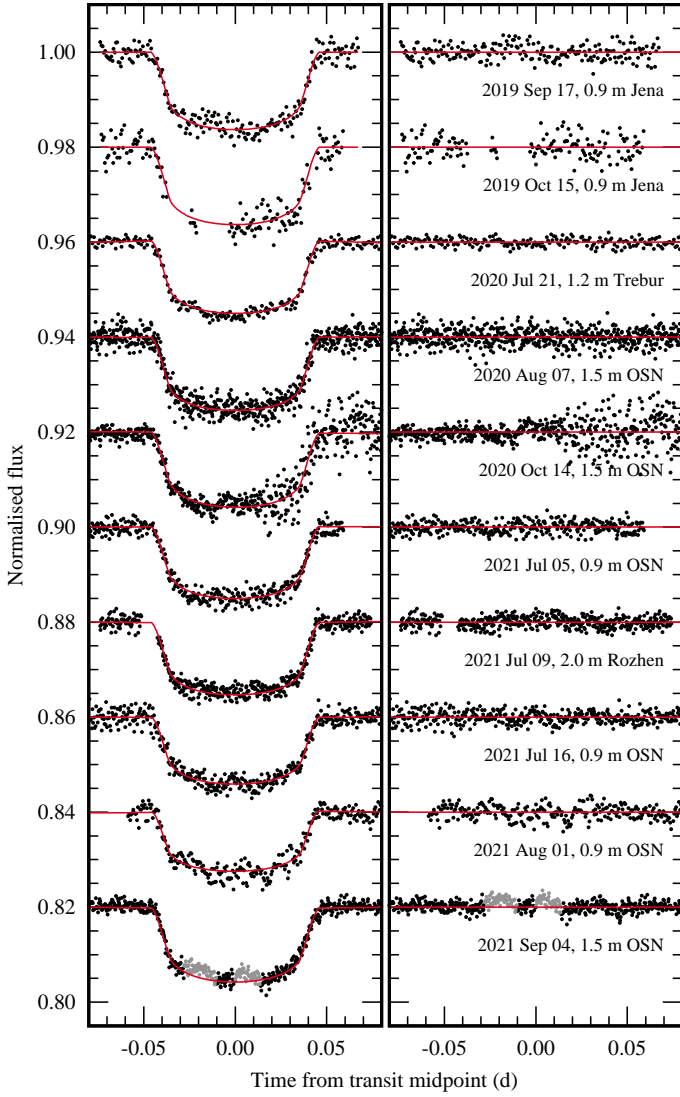


Fig. 1. Left: new transit light curves for HAT-P-23 b, sorted by the observation date. The best-fitting model is drawn with red lines. A signature of star-spot occultation identified in the light curve acquired on 2021 September 04 is marked with grey points. These measurements were masked out in the transit modelling. Right: photometric residuals from the transit model.

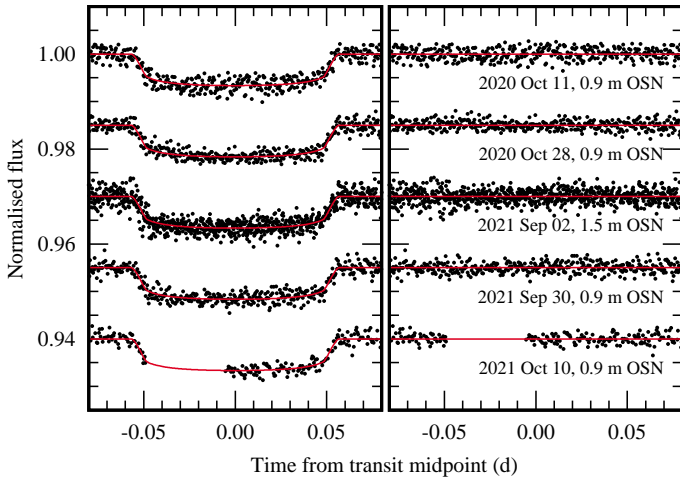


Fig. 2. The same as Fig. 1 but for KELT-1 b.

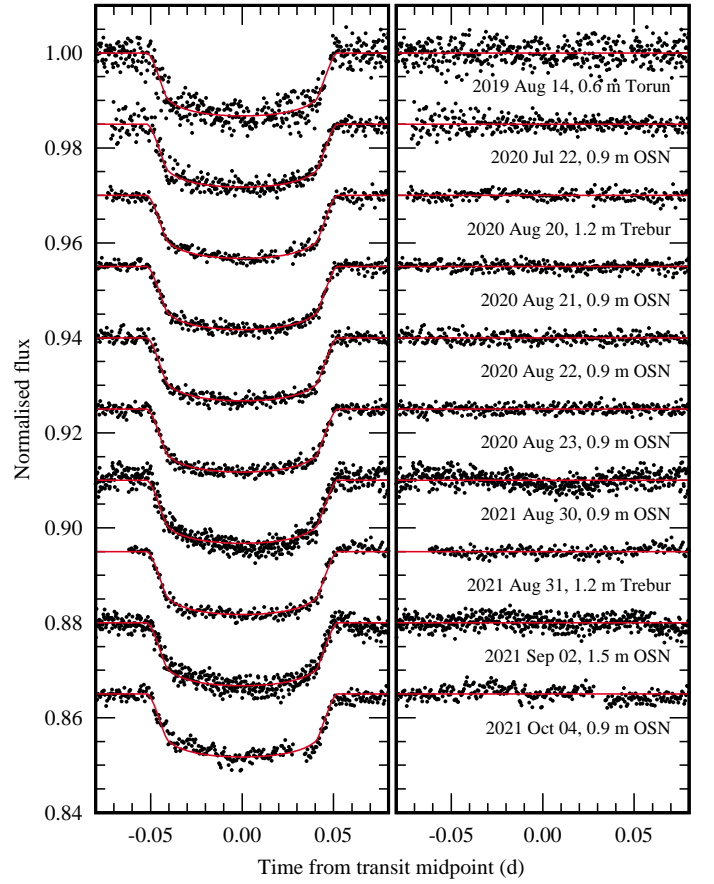


Fig. 3. The same as Fig. 1 but for KELT-16 b.

3. Results

3.1. Transit light curve modeling

The Transit Analysis Package (TAP, Gazak et al. 2012) was employed to model the transit light curves. For each planet, the orbital inclination i_b , the semi-major axis scaled in stellar radii a_b/R_\star , the ratio of planet to star radii R_b/R_\star , the limb darkening coefficients (LDCs) of a quadratic law u_1 and u_2 , times of transit midpoints T_{mid} , and possible flux variations approximated with a second-order polynomial were fitted. The systemic parameters were linked for all light curves. In test runs, we searched for variation in R_b/R_\star in the individual bands, but we found no statistically significant differences. The LDCs for light curves acquired in the same band were also linked. We obtained ground-based and TESS light curve solutions separately in the trial iterations and compared the results. We found no statistically significant differences between these datasets and between the results reported in Maciejewski et al. (2018) and Maciejewski et al. (2020). Thus, in the final iterations, the best-fitting models were found using joint data sets from Maciejewski et al. (2018) and Maciejewski et al. (2020) and the ground-based and TESS light curves which are presented in this paper. This approach allowed us to refine most of the parameters with higher precision. Our tests showed that the greater uncertainties for R_b/R_\star in the HAT-P-23, KELT-1, and WASP-103 systems are caused by allowing u_1 and u_2 to be the free parameters. This approach is advocated by Patel & Espinoza (2022) who have found that discrepancies between the predicted and determined values of TESS LDCs can reach up to $\Delta u \approx 0.2$. The best-fitting parameters and their uncertainties were taken as 50, 15.9, and 84.1 percentiles of the

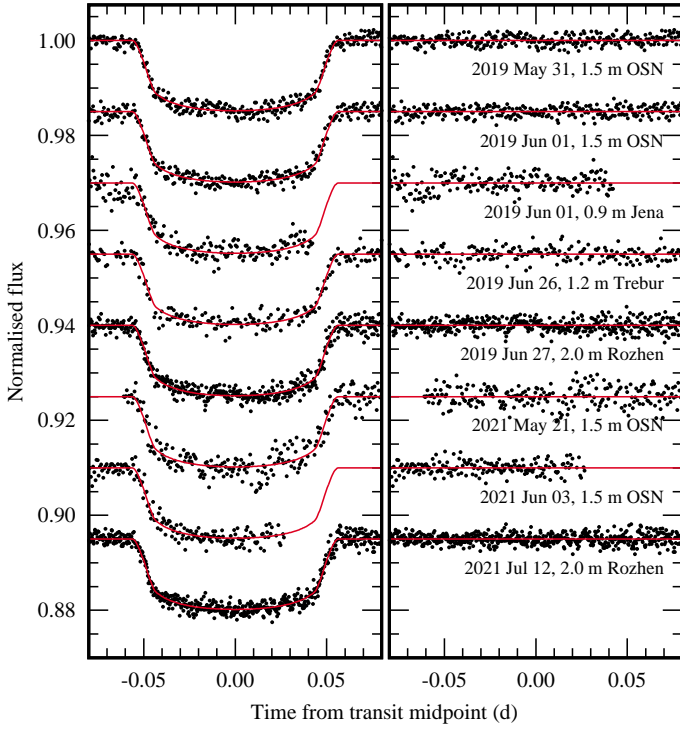


Fig. 4. The same as Fig. 1 but for WASP-103 b.

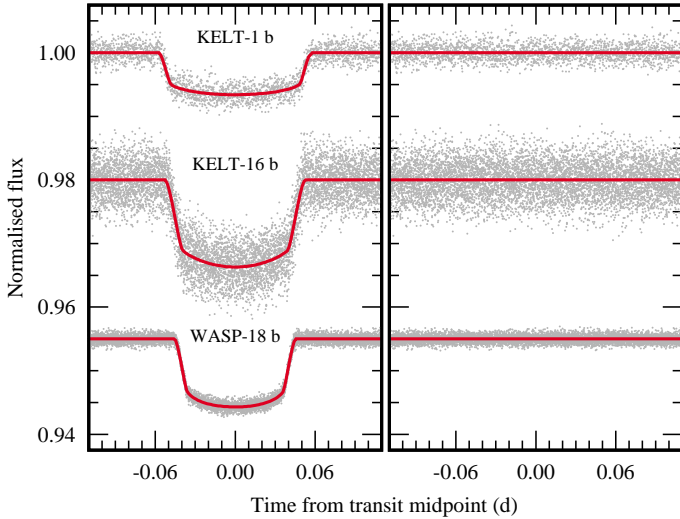


Fig. 5. Left: phase folded TESS transit light curves for KELT-1 b, KELT-16 b, and WASP-18 b. The best-fitting models are plotted with red lines. Right: photometric residuals from the transit models.

marginalised posterior probability distributions generated by ten Markov chains Monte Carlo (MCMC), each 10^6 steps long with a 10% burn-in phase. The results are collected in Table 3 together with some recent literature values for easy comparison. The new values of T_{mid} are given in Table A.1 in Appendix A. The models are sketched in Figs. 1–4 and Fig. 5 together with the residuals.

3.2. Transit timing

Transit timing analysis was performed following the procedure described in Maciejewski et al. (2018). In brief words: Linear transit ephemerides were refined using the updated sets of mid-transit times. We used the new mid-transit times, which are col-

lected in Table A.1 in Appendix A, together with those compiled in Maciejewski et al. (2018) and Maciejewski et al. (2020). For homogeneity, we also redetermined the mid-transit times using publicly available light curves reported in the literature since then. Thus, we enhanced our timing data sets with 27 measurements based on data published by Mancini et al. (2022) for KELT-16 b and with 12 measurements from Barros et al. (2022) for WASP-103 b. The de-trended light curves acquired with the CHAracterising ExOplanet Satellite (CHEOPS) were taken in the latter case. The redetermined transit times are also listed in Table A.1 in Appendix A. Finally, we used a compilation of 38 mid-transit times for HAT-P-23 b, 39 for KELT-1 b, 103 for KELT-16 b, 125 for WASP-18 b, and 51 for WASP-103 b.

The transit timing datasets were used to refine the linear ephemerides in the form

$$T_{\text{mid}}(E) = T_0 + P_{\text{orb}} \cdot E, \quad (3)$$

where E is the transit number counted from the reference epoch T_0 , taken from the discovery paper. The best-fitting parameters and their 1σ were derived with the MCMC technique based on 100 chains, each of which was 10^4 steps long, and the first 1000 trials were discarded. Then, the procedure was repeated for a trial quadratic ephemeris in the form

$$T_{\text{mid}} = T_0 + P_{\text{orb}} \cdot E + \frac{1}{2} \frac{dP_{\text{orb}}}{dE} \cdot E^2, \quad (4)$$

where dP_{orb}/dE is the change of the orbital period between succeeding transits. The Bayesian information criterion (BIC) values were calculated to assess the preferred model. The results are collected in Table 4. The values of the quadratic terms were found to be consistent with zero within $0.3\text{--}1.8\sigma$. The values of BIC also speak in favour of the linear ephemerides for all planets in our sample. The residuals against the refined linear ephemerides are shown in Fig. 6.

Since no statistically significant change of P_{orb} was detected, the 5th percentile of the posterior probability distribution of $\frac{dP_{\text{orb}}}{dE}$ was used to place the lower constraint on Q'_* at the 95% confidence level. We followed Eq. (5) from Maciejewski et al. (2018). The values of the planet-to-star mass ratio M_b/M_* were calculated using the radial velocity amplitudes of the orbital motion K_b following the formula:

$$\frac{M_b}{M_*} = 4.694 \cdot 10^6 \cdot K_b P_b^{1/3} M_*^{-1/3} (\sin i_b)^{-1}, \quad (5)$$

where K_b is in m s^{-1} , P_b is in days, and M_* is in M_\odot . The values of P_b and i_b were taken from this study. The values of K_b and M_* come from the most recent redeterminations, which are available in the literature; they are collected together with the references in Table 5. The errors of the individual parameters were used to estimate the uncertainty for the constraint on Q'_* . The results are given in Table 4.

4. Discussion

For HAT-P-23, Maciejewski et al. (2018) placed the lower constraints on Q'_* equal to $5.6 \cdot 10^5$. Then, it was refined to $(6.4 \pm 1.9) \cdot 10^5$ by Patra et al. (2020). Our constraint of $Q'_* > (2.76 \pm 0.21) \cdot 10^6$ is tighter by a factor of ≈ 4 . More recently, Baştürk et al. (2022) have reported $3.8 \cdot 10^6$ but at a higher confidence level of 99%. For WASP-18 b, precise transit timing observations span over 13 years, making the system the most sensitive probe in the tidal dissipation studies. In the previous study, we eliminated the values of Q'_* lower than $3.9 \cdot 10^6$

Table 3. Systemic parameters refined from transit light curves.

i_b ($^\circ$)	a_b/R_\star	R_b/R_\star	u_1, u_2 (R)	u_1, u_2 (clear)	u_1, u_2 (TESS)	Source
HAT-P-23 b						
$84.45^{+0.44}_{-0.39}$	$4.405^{+0.050}_{-0.049}$	$0.11647^{+0.00076}_{-0.00079}$	$0.32^{+0.10}_{-0.10}, 0.16^{+0.17}_{-0.17}$	$0.54^{+0.09}_{-0.09}, -0.08^{+0.16}_{-0.15}$	—	this paper
$85.23^{+0.54}_{-0.48}$	$4.465^{+0.062}_{-0.059}$	$0.11612^{+0.00058}_{-0.00060}$	$0.35^a, 0.29^a$	$0.40^a, 0.28^a$	—	Mac18
KELT-1 b						
$85.2^{+2.5}_{-1.8}$	$3.58^{+0.11}_{-0.12}$	$0.0766^{+0.0008}_{-0.0008}$	$0.27^{+0.15}_{-0.14}, 0.24^{+0.22}_{-0.24}$	$0.46^{+0.15}_{-0.16}, -0.03^{+0.24}_{-0.23}$	$0.42^{+0.15}_{-0.15}, -0.06^{+0.23}_{-0.23}$	this paper
$85.3^{+2.9}_{-2.6}$	$3.55^{+0.12}_{-0.18}$	$0.0762^{+0.0012}_{-0.0010}$	$0.27^a, 0.33^a$	—	—	Mac18
$85.8^{+2.7}_{-2.8}$	$3.59^{+0.10}_{-0.18}$	$0.07612^{+0.00095}_{-0.00076}$	—	—	$0.26^{+0.09}_{-0.12}, 0.22^{+0.21}_{-0.16}$	Wong21
$87.2^{+1.6}_{-1.6}$	$3.630^{+0.051}_{-0.051}$	$0.0769^{+0.0004}_{-0.0004}$	—	—	$0.319(1)^b, 0.227(3)^b$	vEssen21
—	$3.43^{+0.15}_{-0.09}$	$0.0775^{+0.0007}_{-0.0009}$	—	—	$0.42^{+0.10}_{-0.12}, -0.05^{+0.19}_{-0.14}$	Patel22
KELT-16 b						
$82.87^{+0.70}_{-0.62}$	$3.157^{+0.037}_{-0.035}$	$0.10961^{+0.00065}_{-0.00065}$	$0.49^{+0.12}_{-0.13}, 0.10^{+0.18}_{-0.17}$	$0.41^{+0.07}_{-0.07}, 0.07^{+0.13}_{-0.13}$	$0.40^{+0.10}_{-0.09}, 0.03^{+0.15}_{-0.15}$	this paper
$84.5^{+2.0}_{-1.4}$	$3.238^{+0.084}_{-0.075}$	$0.1076^{+0.0010}_{-0.0010}$	$0.29^a, 0.32^a$	$0.36^a, 0.29^a$	—	Mac18
$84.8^{+3.0}_{-3.3}$	$3.21^{+0.10}_{-0.16}$	$0.1099^{+0.0021}_{-0.0019}$	—	—	$0.23^{+0.12}_{-0.13}, 0.34^{+0.28}_{-0.22}$	Wong21
$89.72^{+0.25}_{-0.25}$	$3.319^{+0.022}_{-0.022}$	$0.10814^{+0.00087}_{-0.00087}$	—	—	—	Mancini22
WASP-18 b						
$83.97^{+0.31}_{-0.31}$	$3.487^{+0.020}_{-0.020}$	$0.09777^{+0.00022}_{-0.00022}$	—	—	$0.294^{+0.027}_{-0.026}, 0.172^{+0.047}_{-0.050}$	This paper
$84.04^{+0.36}_{-0.38}$	$3.492^{+0.024}_{-0.025}$	$0.09776^{+0.00028}_{-0.00027}$	—	—	$0.296^{+0.034}_{-0.034}, 0.159^{+0.061}_{-0.060}$	Mac20
$84.88^{+0.33}_{-0.33}$	$3.562^{+0.022}_{-0.023}$	$0.09716^{+0.00014}_{-0.00013}$	—	—	$0.219^c, 0.313^c$	Shporer19
WASP-103 b						
$86.5^{+1.9}_{-1.4}$	$2.977^{+0.031}_{-0.037}$	$0.11255^{+0.00076}_{-0.00072}$	$0.23^{+0.12}_{-0.12}, 0.30^{+0.18}_{-0.18}$	$0.35^{+0.06}_{-0.07}, 0.17^{+0.12}_{-0.12}$	—	this paper
$87.9^{+1.4}_{-1.7}$	$2.996^{+0.018}_{-0.033}$	$0.11204^{+0.00070}_{-0.00070}$	$0.31^a, 0.31^a$	$0.36^a, 0.30^a$	—	Mac18
$87.0^{+0.2}_{-0.2}$	$3.01^{+0.01}_{-0.01}$	$0.1136^{+0.0005}_{-0.0005}$	—	—	—	Kirk21

Notes. ^a interpolated from the theoretical tables of Claret & Bloemen (2011) and varied under the Gaussian penalty of the width of 0.1. ^b calculated from PHOENIX library and kept fixed in modeling. ^c fixed at the theoretical values interpolated from the tables of Claret (2017). Data source: Kirk21 – Kirk et al. (2021), Mac18 – Maciejewski et al. (2018), Mac20 – Maciejewski et al. (2020), Mancini22 – Mancini et al. (2022), Patel22 – Patel & Espinoza (2022), Shporer19 – Shporer et al. (2019), vEssen21 – von Essen et al. (2021), the circular-orbit solution, Wong21 – Wong et al. (2021).

Table 4. Parameters of the refined transit ephemerides.

Planet	T_0 (BJD _{TDB})	P_{orb} (d)	$\frac{dP_{\text{orb}}}{dE} (-\cdot 10^{-10})$	N_{dof}	χ^2	BIC	$Q'_* >$
linear ephemerides							
HAT-P-23 b	2454852.26528(13)	1.212886436(52)	—	46	32.6	40.3	—
KELT-1 b	2455909.29304(25)	1.21749391(12)	—	36	29.2	36.4	—
KELT-16 b	2457247.24798(13)	0.968992922(82)	—	101	117.1	126.4	—
WASP-18 b	2454221.481843(74)	0.941452411(16)	—	123	104.6	114.3	—
WASP-103 b	2456459.599285(77)	0.925545423(42)	—	49	54.7	62.6	—
trial quadratic ephemerides							
HAT-P-23 b	2454852.26545(18)	1.21288621(17)	1.14 ± 0.82	45	30.7	40.3	$2.76^{+0.21}_{-0.21} \cdot 10^6$
KELT-1 b	2455909.29291(30)	1.21749427(44)	-2.5 ± 2.9	35	28.6	39.5	$2.33^{+0.36}_{-0.38} \cdot 10^6$
KELT-16 b	2457247.24765(24)	0.96899357(40)	-5.2 ± 2.9	100	114.3	128.2	$2.95^{+0.23}_{-0.23} \cdot 10^5$
WASP-18 b	2454221.48181(12)	0.94145244(9)	-0.09 ± 0.28	122	104.5	119.0	$1.09^{+0.04}_{-0.04} \cdot 10^7$
WASP-103 b	2456459.59941(13)	0.92554517(21)	1.6 ± 1.3	48	53.2	65.0	$3.74^{+0.28}_{-0.31} \cdot 10^6$

Notes. Uncertainties of T_0 and P_{orb} are given in the concise notation. N_{dof} is the number of degrees of freedom. $Q'_* >$ is the the lower constraint at the 95% confidence level.

(Maciejewski et al. 2020). In this study, we push this constraint to $Q'_* > (1.09 \pm 0.04) \cdot 10^7$. In the case of the WASP-103 system, the results of Maciejewski et al. (2018), Patra et al. (2020), and Barros et al. (2022) showed that the orbital period of the giant planet could increase. The presence of a third body in the system or apsidal precession was postulated to explain that finding. Because of that apparently positive derivative of P_{orb} , Maciejewski et al. (2018) and Barros et al. (2022) could place constraints on Q'_* only with higher confidence levels: 10^6 at 99.96% and $1.6 \cdot 10^6$ at 99.7%, respectively. Patra et al. (2020) reported a rather weak constraint with $Q'_* > (1.1 \pm 0.1) \cdot 10^5$ at 95%

confidence. However, the statistical significance of the reported positive period derivative appears to decrease as the span of observations widens. Our new observations allowed us to place the tighter constraint of $Q'_* > 3.74^{+0.28}_{-0.31} \cdot 10^6$ with no statistically significant change in the orbital period of WASP-103 b.

If the mechanism of internal gravity wave dissipation operated in the host stars of these three systems, the orbital period shortening could likely be detected in current transit timing data. For HAT-P-23, WASP-18, and WASP-103, the predicted values of Q'_{IGW} are $3.5 \cdot 10^5$, $2.6 \cdot 10^6$, and $4 \cdot 10^5$, respectively (Barker 2020). Our empirical limits on Q'_* are greater up to one order

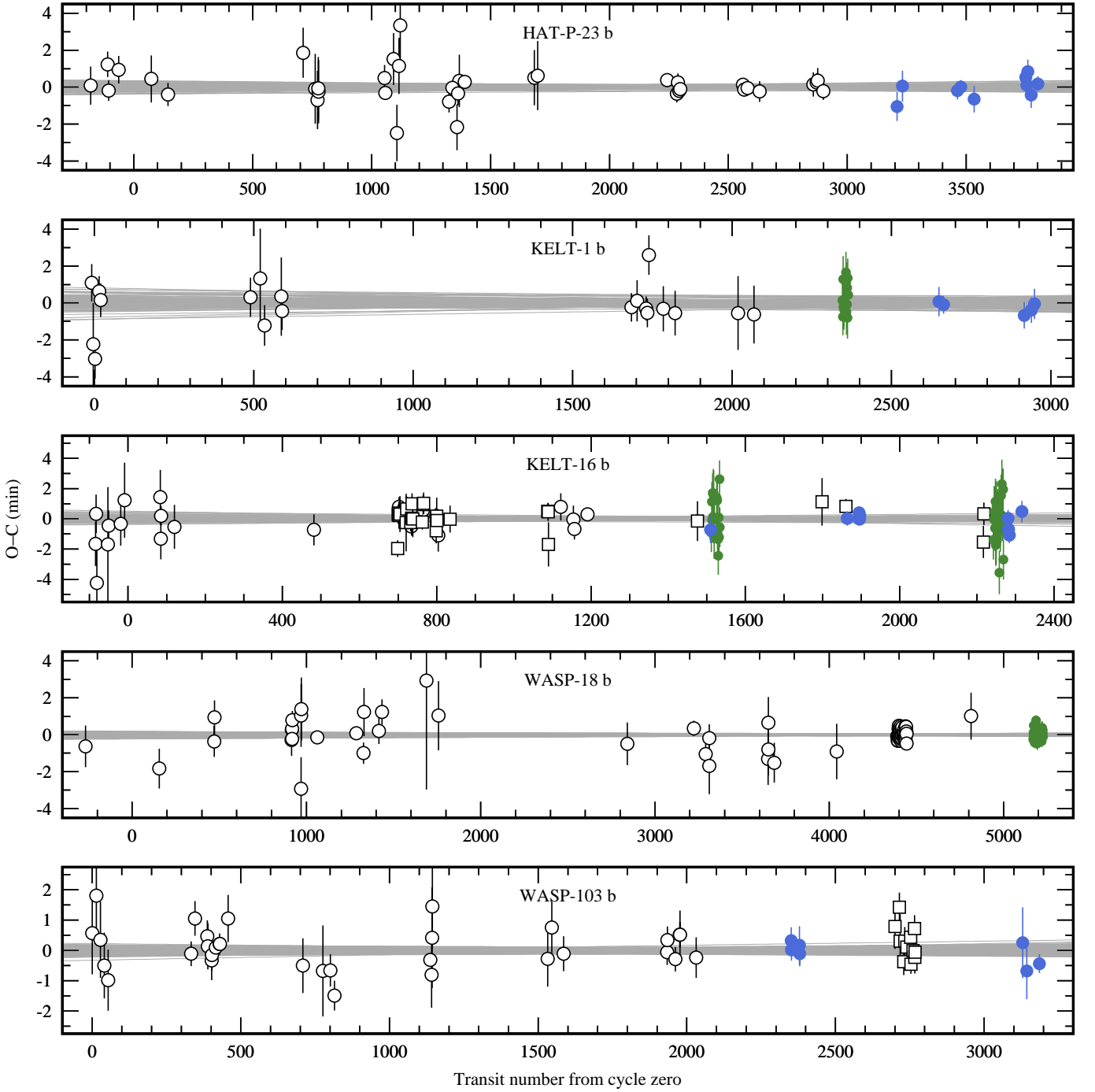


Fig. 6. Transit timing residuals for the planets of our sample. The open circles mark the data compiled in Maciejewski et al. (2018) and Maciejewski et al. (2020). Open squares are the new literature mid-points redetermined in this study (for Kelt-16 b and WASP-103 b). The filled dots are the new determinations reported in this paper: the green and blue points come from TESS and ground-based photometry, respectively. The uncertainties of the refined ephemerides are illustrated with bunches of 100 lines, each drawn from the Markov chains.

of magnitude. As predicted by models of Barker (2020), wave breaking does not happen in these stars, preventing their planets from rapid orbital decay.

KELT-16 b has the shortest observational coverage among our sample objects, which results in the weakest constraint on Q'_* . Maciejewski et al. (2018) and Patra et al. (2020) reported the consistent values of $1.1 \cdot 10^5$ and $(0.9 \pm 0.2) \cdot 10^5$, respectively. More recently, Mancini et al. (2022) used the TESS data from Sector 15 and the additional ground-based observations to push this constraint to $(2.2 \pm 0.4) \cdot 10^5$. Our timing dataset yields a tighter constraint of $(2.95 \pm 0.23) \cdot 10^5$. This results is still too

weak to address tidal boosting because the theoretical prediction is $Q'_{\text{IGW}} = 7 \cdot 10^5$ (Barker 2020). As the mass of the star is $\approx 1.2 M_\odot$ (Mancini et al. 2022), this tidal boost is, however, improbable.

The KELT-1 system was recognised as the best candidate for studying the star-planet tidal interaction (Maciejewski et al. 2018) unless the stellar spin is synchronised to the orbital period. The rotation period of the host star was found to be equal to $P_* = 1.33 \pm 0.06$ d from the measured projected rotation velocity (Siverd et al. 2012) and $P_* = 1.52 \pm 0.29$ d from photometric variations (von Essen et al. 2021). Both results differ by more

Table 5. Literature parameters of the systems under investigation.

System	K_b (m s ⁻¹)	source	M_\star (M_\odot)	source
HAT-P-23	368.5 ± 17.6	Ciceri et al. (2015)	1.104 ± 0.047	Ciceri et al. (2015)
KELT-1	4239 ± 52	Siverd et al. (2012)	1.34 ± 0.08	von Essen et al. (2021)
KELT-16	494 ± 25	Oberst et al. (2017)	1.195 ± 0.044	Mancini et al. (2022)
WASP-18	1813.9 ± 2.4	Maciejewski et al. (2020)	$1.294^{+0.063}_{-0.061}$	Cortés-Zuleta et al. (2020)
WASP-103	268 ± 14	Barros et al. (2022)	1.204 ± 0.046	Barros et al. (2022)

than 1σ from the orbital period of KELT-1 b, which is 1.22 d. Thus, the spin and orbit synchronisation may still be ongoing. The tidal period in the KELT-1 system is ≈ 7 days and is longer than half the host star's rotation. In such a configuration, tidal dissipation might be enhanced by interactions of inertial waves and turbulent motions in a convective layer of the star. Since an analytic formula that estimates the theoretical value of Q'_{IW} is not available we utilised Figs. 4 and 6 of Barker (2020) to find $Q'_{IW} \approx 2.6 \cdot 10^6$ for KELT-1. Our empirical constraint of $2.33^{+0.36}_{-0.38} \cdot 10^6$ does not reject this value. We also calculated Q'_{IGW} using Equation (44) from Barker (2020). Its value of $\approx 5 \cdot 10^8$ is well beyond the detection limit of current and near-future transit timing observations.

5. Conclusions

Our transit timing data show that tidal dissipation is not boosted by breaking internal gravity waves in HAT-P-23, WASP-18, and WASP-103 host stars. This negative result is in line with the models of stellar interiors of stars with masses above $1.1 M_\odot$ for which convective cores prevent the waves from reaching the stellar centres and breaking. For KELT-16, the span of observations is not long enough to verify the theoretical predictions yet. Precise transit timing in the following years will allow us to probe the regime of dynamical tides in that system.

The KELT-1 system was found not to be a favourable laboratory for studying tidal dissipation if the equilibrium tides or internal gravity wave mechanisms are considered. However, it might become a unique tool for probing the dissipative tidal interactions of inertial waves in convective layers. Further observations will help us to explore that scenario.

Acknowledgements. We thank the anonymous referee for the comments that improved the quality of this paper. GM acknowledges the financial support from the National Science Centre, Poland through grant no. 2016/23/B/ST9/00579. MF and PJA acknowledge financial support from grant PID2019-109522GB-C5X/AEI/10.13039/501100011033 of the Spanish Ministry of Science and Innovation (MICINN) and from grant P20-00737 of the Andalusian Government program PAIDI 2020. MF, AS, and PJA acknowledge financial support from the State Agency for Research of the Spanish MCIU through the *Center of Excellence Severo Ochoa* award to the Instituto de Astrofísica de Andalucía (SEV-2017-0709). MM and RB acknowledge the support of the DFG priority programme SPP 1992 *Exploring the Diversity of Extrasolar Planets* (NE 515/58-1 and MU 2695/27-1). This paper includes data collected with the TESS mission, obtained from the MAST data archive at the Space Telescope Science Institute (STScI). Funding for the TESS mission is provided by the NASA Explorer Program. STScI is operated by the Association of Universities for Research in Astronomy, Inc., under NASA contract NAS 5-26555. This research made use of Lightkurve, a Python package for Kepler and TESS data analysis (Lightkurve Collaboration et al. 2018). This research has made use of the SIMBAD database and the VizieR catalogue access tool, operated at CDS, Strasbourg, France, and NASA's Astrophysics Data System Bibliographic Services.

References

Baştürk, Ö., Esmer, E. M., Yalçinkaya, S., et al. 2022, MNRAS[arXiv:2203.00299]

Barker, A. J. 2020, MNRAS, 498, 2270
 Barros, S. C. C., Akınanmi, B., Boué, G., et al. 2022, A&A, 657, A52
 Brown, D. J. A. 2014, MNRAS, 442, 1844
 Ciceri, S., Mancini, L., Southworth, J., et al. 2015, A&A, 577, A54
 Claret, A. 2017, A&A, 600, A30
 Claret, A. & Bloemen, S. 2011, A&A, 529, A75
 Collins, K. A., Kielkopf, J. F., Stassun, K. G., & Hessman, F. V. 2017, AJ, 153, 77
 Cortés-Zuleta, P., Rojo, P., Wang, S., et al. 2020, A&A, 636, A98
 Fulton, B. J., Shporer, A., Winn, J. N., et al. 2011, AJ, 142, 84
 Gazak, J. Z., Johnson, J. A., Tonry, J., et al. 2012, Advances in Astronomy, 2012, 697967
 Gillon, M., Anderson, D. R., Collier-Cameron, A., et al. 2014, A&A, 562, L3
 Hamer, J. H. & Schlaufman, K. C. 2019, AJ, 158, 190
 Hellier, C., Anderson, D. R., Collier Cameron, A., et al. 2009, Nature, 460, 1098
 Kirk, J., Rackham, B. V., MacDonald, R. J., et al. 2021, AJ, 162, 34
 Lightkurve Collaboration, Cardoso, J. V. d. M., Hedges, C., et al. 2018, Lightkurve: Kepler and TESS time series analysis in Python
 Maciejewski, G., Fernández, M., Aceituno, F., et al. 2018, Acta Astron., 68, 371
 Maciejewski, G., Knutson, H. A., Howard, A. W., et al. 2020, Acta Astron., 70, 1
 Mancini, L., Southworth, J., Naponiello, L., et al. 2022, MNRAS, 509, 1447
 Maxted, P. F. L., Serenelli, A. M., & Southworth, J. 2015, A&A, 577, A90
 Mugrauer, M. & Berthold, T. 2010, Astronomische Nachrichten, 331, 449
 Oberst, T. E., Rodriguez, J. E., Colón, K. D., et al. 2017, AJ, 153, 97
 Patel, J. A. & Espinoza, N. 2022, AJ, 163, 228
 Patra, K. C., Winn, J. N., Holman, M. J., et al. 2020, AJ, 159, 150
 Ricker, G. R., Winn, J. N., Vanderspek, R., et al. 2014, in Society of Photo-Optical Instrumentation Engineers (SPIE) Conference Series, Vol. 9143, Space Telescopes and Instrumentation 2014: Optical, Infrared, and Millimeter Wave, ed. J. Oschmann, Jacobus M., M. Clampin, G. G. Fazio, & H. A. MacEwen, 914320
 Shporer, A., Wong, I., Huang, C. X., et al. 2019, AJ, 157, 178
 Siverd, R. J., Beatty, T. G., Pepper, J., et al. 2012, ApJ, 761, 123
 Southworth, J., Hinse, T. C., Jørgensen, U. G., et al. 2009, MNRAS, 396, 1023
 Tejada Arevalo, R. A., Winn, J. N., & Anderson, K. R. 2021, ApJ, 919, 138
 von Essen, C., Mallonn, M., Piette, A., et al. 2021, A&A, 648, A71
 Wong, I., Kitzmann, D., Shporer, A., et al. 2021, AJ, 162, 127

Appendix A: New mid-transit times

The transit mid-points obtained from the new transit light curves and those that are available in the literature are collected in Table A.1. They were combined with timing datasets from Maciejewski et al. (2018) and Maciejewski et al. (2020) for transit timing studies based on homogeneously determined data.

Table A.1. Mid-transit times reported in this paper.

T_{mid} (BJD _{TDB})	$+\sigma$ (d)	$-\sigma$ (d)	Light curve
HAT-P-23 b			
2458744.417125	0.000547	0.000544	Jena
2458772.314281	0.000581	0.000583	Jena
2459052.490879	0.000329	0.000347	Trebur
2459069.471419	0.000261	0.000264	OSN150
2459137.392604	0.000495	0.000491	OSN150
2459400.589783	0.000293	0.000295	OSN90
2459405.441030	0.000300	0.000308	Rozhen
2459411.505979	0.000443	0.000447	OSN90
2459428.485508	0.000483	0.000457	OSN90
2459462.446747	0.000290	0.000285	OSN150
KELT-1 b			
...